

# Development of the ‘GP2’ detector: Modification of the PImMS CMOS Sensor for Energy Resolved Neutron Radiography

*D. E. Pooley, J. W. L. Lee, M. Brouard, J. J. John, W. Kockelmann, N. J. Rhodes, E. M. Schooneveld,  
I. Sedgwick, R. Turchetta, C. Vallance*

**Abstract**—This paper reports on the development and commissioning of the GP2 detector. GP2 was developed to address the requirement for a high resolution event-mode imaging detector, for application in energy resolved neutron radiography. The name GP2 derives from the use of gadolinium as a neutron conversion material, combined with a second-generation mass spectrometry sensor known as PImMS2. Theoretical and measured characteristics of GP2 are compared, with emphasis on the usability and functionality of the detector. The development of the detector has been steered by a design philosophy which was established to ensure that the detector has unique and novel impact. The motivation and consequences of the design philosophy are discussed. The key parameters reported are the neutron detection efficiency (7.5 % at 2.5 Å), gamma sensitivity ( $1.5 \times 10^{-3}$ ) and a spatial resolution (modulation transfer function at 10 %) of 6.4 lp/mm for a 4 µm thick natural gadolinium neutron converter film.

**Index Terms**—Energy resolved neutron radiography, CMOS, gadolinium, tomography, Time-of-flight, neutron, imaging, PImMS, ERNR.

## I. MOTIVATION

WHITE beam neutron radiography (WBNR) is a well-established nondestructive technique, with the first images being collected in 1935 [1] [2]. The grey-scale radiographs provide quantitative information as the contrast variation is proportional to the beam attenuation. In the simplest case, beam attenuation can be modelled as a function of path length, density and the total neutron cross section. Furthermore, as the absorption and scattering cross sections are unique and not proportional to atomic number, measurements of systems with similar atomic number are routinely performed. This extends to the light isotopes, for

which interactions with elements such as lithium and hydrogen can be measured and distinguished, especially when the method of isotope substitution is implemented. For these reasons WBNR is often utilized by the hydrogen fuel-cell community [3] [4], for nuclear fuel assay [5], and more recently for phytology [6]. Being a nondestructive method with the ability to probe internal structure, WBNR has also found a niche in cultural heritage studies [7], archaeology [8], and paleontology [9] [10]. While WBNR utilizes the isotope dependency of the neutron cross sections, the energy dependence of the neutron transmission is effectively averaged out. To access this information the measurement must be performed at a range of neutron energies, in so-called *energy resolved neutron radiography* (ERNR). ERNR encapsulates a broad category of neutron imaging methods, and covers all techniques that require the measurement of the energy dependence of the transmission spectrum. By measuring the neutron energy, much more information about the sample can be obtained. This includes, but is not limited to, crystalline texture, material phase, strain and temperature.

ERNR is particularly suited to pulsed neutron spallation sources, for which the neutron energy is measured by the time-of-flight (ToF) technique [11]. However, despite a wealth of proof-of-principle studies [12] [13] [14] [15], the technique is considered to be under-utilized at these facilities, for reasons often attributed primarily to the lack of suitable detector technology [16]. This conclusion is drawn when one considers the ideal specification for a viable ERNR detector. Developing a detector that provides a suitably high spatial and temporal resolution, neutron detection efficiency, detection area and minimal has only recently become feasible. While there are detector technologies that meet several of the individual specifications, it is the requirement for all these properties in one detector that is challenging. The pioneering detector in this field was developed by Tremsin *et al.* [17]. The current version of this detector uses four TimePix sensors butted together and coupled to a neutron-sensitive micro-channel plate [18].

The GP2 detector, reported here, has been developed using alternative technologies, with the aim of providing an independent and complementary detector solution to those currently available. This paper documents the design details, the measured detector properties and explains the justification

Manuscript submitted June, 2017. This work was supported in part by the STFC Centre for Instrumentation and EPSRC programme grant EP/L005913/1.

D. E. Pooley, N. J. Rhodes, E. M. Schooneveld, R. Turchetta, I. Sedgwick and W. Kockelmann are with STFC, Rutherford Appleton Laboratory, Harwell Oxford, Didcot, OX11 0QX, UK, (e-mail: author.daniel.pooley@stfc.ac.uk).

J. W. L. Lee, M. Brouard and C. Vallance are with Department of Chemistry, Chemistry Research Laboratory, 12 Mansfield Rd, University of Oxford, Oxford, UK, (e-mail: jason.lee@chem.ox.ac.uk).

J. J. John is with Department of Physics, Denys Wilkinson Building, Keble Rd, University of Oxford, Oxford, UK, (e-mail: j.john1@physics.ox.ac.uk).

for the design choices made. Where appropriate, clarification is provided over terminology and methodology to aid the reader when comparing established detector technology, such as CCDs, with this new class of detector.

A sketch of the setup of a typical ERNR measurement with the GP2 detector is shown in Fig 1. The Figure illustrates both the energy dependence of the beam attenuation and the geometry of the experiment. The GP2 detector, introduced later in §III, is also illustrated. For reference, the detector is shown in ‘forward’ geometry, with the detector facing the incoming neutron beam, explained in detail in §III. GP2 consists of a neutron-sensitive CMOS sensor housed in a camera body, controlled by bespoke software. These elements are detailed individually in §IV. Here, attention is drawn to the fact that each neutron is individually and uniquely tagged in position and time within each neutron pulse. The term *neutron pulse* is used here to describe the neutron spectrum arriving at a detector, which is placed at a known distance from the moderator. The temporal spread (time of flight) is a simple relationship to the kinetic energy distribution of the neutrons, combined with the flight path distance. The term *frame*, or *frame length*, is used to describe the time the detector is actively recording data. This may be shorter or longer than the period defined by the source pulse rate. For example, a detector may be set to record an 80 ms frame, from a source that has repetition rate of 10 Hz. For the remaining 20 ms, the detector is not recording data. At a dedicated ERNR instrument, such as IMAT at the ISIS pulsed neutron and muon source [19], the neutron pulse is generated and moderated every 100 ms and the flightpath is 56 m.

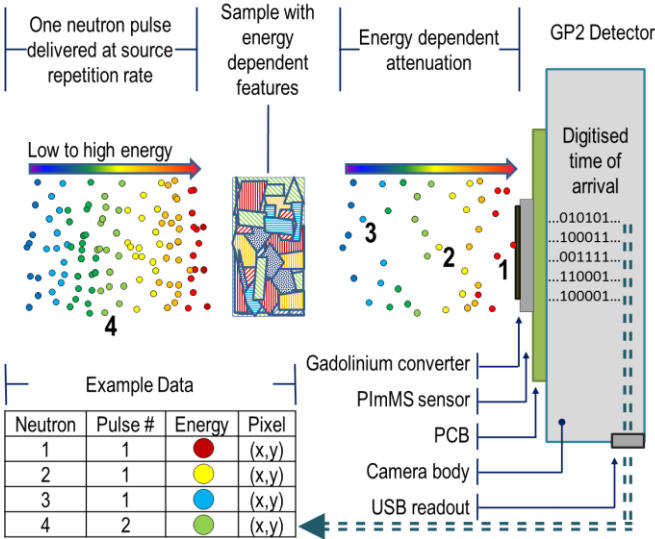


Fig 1. Sketch illustrating the energy dependent beam attenuation, as measured in a typical ERNR experiment. The GP2 detector records every neutron’s arrival time, giving the energy of that neutron and its (x,y) position. Four neutrons, labelled 1-4, from two separate neutron pulses are labelled to illustrate and emphasize this point.

## II. DETECTOR REQUIREMENTS AND DESIGN PHILOSOPHY

The GP2 detector was developed to meet the specification

for ERNR at an imaging beamline on a pulsed spallation source. These specifications are well documented in the literature and broadly consistent across the facilities [19] [20] [21]. Generally speaking, a high performance ERNR beamline would specify a spatial resolution better than 100  $\mu\text{m}$ , temporal sampling faster than 100  $\mu\text{s}$ , and the largest possible detector area. Area coverage is not straight-forward to specify if the spatial and temporal resolution are fixed as above. In this case, a detector above 20 mm x 20 mm would be considered large even though this area is a small fraction of the beam size, typically 200 mm x 200 mm. If a full-beam image is required a compromise has to be made. For example, a high spatial resolution CCD imaging system can be used, which has no intrinsic energy resolution, or a time-of-flight capable detector with larger pixels [22]. There are also a number of more flexible criteria which affect usability, data reduction and ultimately the user experience. Accordingly, the development pathway for GP2 was steered with these requirements in mind, by adopting the following design philosophy:

### 1) Active Area

The active area should be truly continuous, without gaps or dead regions. This is to minimize potential reconstruction problems in tomographic studies.

### 2) Compactness and Robustness

The detector should be as small and compact as possible, free of moving parts and use few fragile components. This allows it to be fitted to existing beamlines retroactively, where imaging or beam diagnostics are now desired.

### 3) Portability

The detector should not require a vacuum or cooling to operate. While this could be a later addition to enhance performance, the standard operating mode should not require additional components such as a vacuum pump, Peltier cooler or cold finger. This again facilitates retroactive fitting to an existing beamline and also impromptu or on-the-fly measurements in novel geometries.

### 4) Diagnostics and Communication

The detector should be developed with hardware and software-level diagnostics tools that are accessible to the non-expert user. Wherever possible, standardized connectivity and communication should be implemented.

The selection of detector hardware, neutron conversion mechanism and detector functionality were all made with these principles in mind. For clarity each of these components is described separately in the following sections.

## III. INTRODUCTION TO GP2 AND OVERVIEW

After review of the specification for ERNR, a detector solution using a monolithic CMOS sensor was deemed the most suitable. The sensor selected is known as the PImMS sensor and is described in §IV.B. The PImMS sensor has been made neutron sensitive by sputtering a thin-film of gadolinium onto the sensor surface, as seen in Fig 2. In this application, the thin film has a thickness in the range from 1  $\mu\text{m}$  to 10  $\mu\text{m}$ .

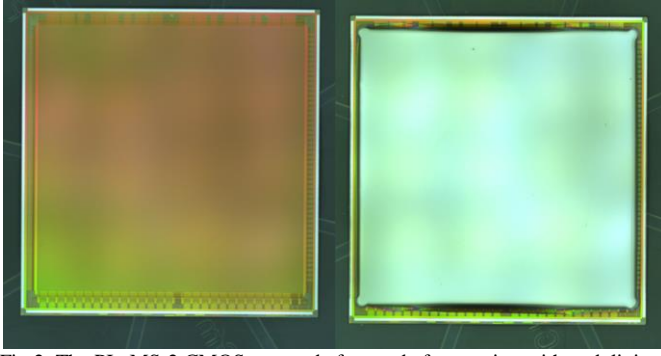


Fig 2. The PImMS-2 CMOS sensor, before and after coating with gadolinium. The coating shown is 7  $\mu\text{m}$  thick.

The gadolinium layer has been made thin enough for the detector to operate in ‘forward’ geometry, depicted in Fig 1. In forward geometry the neutrons first impinge on the gadolinium layer and the sensor registers the conversion electrons that are transmitted through the remaining gadolinium, into the sensor. The detector can also operate in *reverse* geometry, where the neutrons first pass through the whole detector assembly, including the PImMS sensor, which records electrons ejected back towards the incoming beam. The merits of these geometries are discussed later in §VI.A. The coating process does not affect the operational performance of the sensor, with the exception and advantage of it becoming optically blind.

Gadolinium was selected as a conversion material due to the high neutron conversion efficiency. Furthermore, gadolinium produces conversion electrons with a range comparable (or less than) the PImMS pixel size, minimizing multi-counting and clustering (in which multiple adjacent pixels are triggered by a single neutron). A scintillator-based approach was not adopted as tests found that clustering increased when coupling PImMS with LiF/ZnS imaging scintillators. Surface treatment techniques designed to increase efficiency, such as trenching, are not compatible with this sensor. An additional benefit of coating the sensor surface is that the sensor does not need to be inside a light-tight enclosure. If desired, the user could place the sensor within 2 mm of the sample providing due care is taken. However, the optimum sample-sensor gap is governed by the instrument profile and the nature of the sample being measured, meaning that a very small gap is often not required. One clear disadvantage of using gadolinium is the lack of sensitivity for epithermal neutrons.

#### IV. GP2 CHARACTERISTICS

##### A. Neutron Conversion via Gadolinium

Gadolinium has the largest neutron capture cross section of all the stable elements. For example  $^{157}\text{Gd}$  has a thermal neutron cross section of 49700 b at 1.8  $\text{\AA}$ , which can be compared to that of  $^3\text{He}$  (5333 b) or  $^{10}\text{B}$  (3835 b) [23]; two other isotopes commonly used as conversion materials. On capture of a neutron, the gadolinium nucleus emits a spectrum of gamma rays, which in turn generate conversion electrons,

X-rays and Auger electrons [24] [25]. Across the literature there is discrepancy as to the precise shape of the conversion electron spectrum. For example, Abdushukurov *et al.* calculate that the intensity of the  $^{157}\text{Gd}$  131.7 keV and 71.7 keV lines are comparable [26], while Varner *et al.* report minimal intensity above  $\sim 90$  keV [27]. The most recent modeling of the conversion process was performed by Pfeiffer *et al.* [28], for  $^{157}\text{Gd}$ , who concluded that the majority of electrons are liberated in two energy bands, one around 29 keV and the other around 70 keV. This is broadly consistent with both

TABLE I  
SPECIFICATION OF THE PIMMS-2 CMOS SENSOR

Parameter	Value
Pixel size	70 x 70 $\mu\text{m}$
Pixel number	324 x 324 = 104976
Active area	22.7 mm x 22.7 mm
Bit depth (time bins available)	12 bit (maximum 4095)
Smallest temporal bin width	12.5 ns
Registers per pixel	4

Selected parameters of the PImMS sensor, relevant to ERNR.

Abdushukurov *et al* and Varner *et al*, who attribute these energies to K and L shell emissions. To achieve the highest possible neutron detection efficiency, the detector system must be sensitive to electrons across this energy range. For GP2 to detect the conversion electrons, they must first escape the gadolinium and deposit enough energy into the depletion region of the sensor to trigger the pixel. The depletion region, comprising the charge collection diodes, is approximately 15  $\mu\text{m}$  under the sensor surface. The combination of the short range of the conversion electrons and the sensor properties results in a neutron detection efficiency that is strongly dependent on the thickness of gadolinium employed. Characteristic efficiency curves have been calculated [29] for a range of incident neutron energies. For a detector system in forward geometry (in which the detected electrons are measured from the opposite surface to the incident neutrons) there is a maximum in efficiency as a function of gadolinium layer thickness, typically at thicknesses in the range from 4  $\mu\text{m}$  to 5  $\mu\text{m}$  for 2  $\text{\AA}$  neutrons. The exact peak in efficiency must be validated experimentally, as not only are these processes difficult to model, but detector efficiency is always a trade-off between dependent parameters such as thermal noise, gamma sensitivity and stability. The optimization of the Gd thickness will be published separately, as this is considered to be a separate study. The results reported here are for an optimized 4  $\mu\text{m}$  thick  $^{157}\text{Gd}$  film sputtered directly onto the PImMS CMOS surface. Potential increases in detector efficiency are discussed in §VIII.A in the context of future work.

##### B. The PImMS CMOS Sensor

The GP2 detector utilizes the PImMS CMOS sensor, named for its originally-intended application of Pixel Imaging Mass Spectrometry, a novel form of imaging mass spectrometry for studying molecular fragmentation events and performing

molecular imaging of surfaces. The PImMS chip is a monolithic sensor; it is not comprised of sensors butted or stitched together. Selected technical specifications relevant to ERNR are provided in Table I, such as pixel size, active area and temporal binning parameters. Comprehensive details about the PImMS sensor and its development are found in [30] [31].

The PImMS sensor operates in ‘event-mode’, in which triggering of a pixel generates a timecode for the registered neutron via a set of four 12-bit counters located within each pixel. This means that every neutron is assigned a position (based on the pixel location) and a unique time-code. As each pixel has four 12-bit SRAM memory registers, up to four neutrons can be recorded per pixel per frame. While bit-depth indicates the dynamic range (or grey scale) for a CCD based detector here it is the maximum number of time-bins available in a given frame. A 0-value in a register indicates the special state ‘not hit’, while any pixel that has been triggered during an acquisition cycle will contain a value between 1 and 4095. The temporal width of each time bin is set by the user to be an integer multiple of the primary clock, which has a period of 12.5 ns. Selection of this multiple depends on the required frame length. For example, if a frame length of 20 ms was required, the optimum time bin width would be  $20 / 4095 = \sim 5 \mu\text{s}$ , corresponding to a multiple of 400.

More complex measuring strategies are discussed in §V.B.

### C. Combining Gadolinium and PImMS

The process of sputtering gadolinium onto the surface of the PImMS sensor was initially optimized using silicon wafer substrates. This work had two aims: firstly, to ensure that stable, robust films could be deposited onto silicon. Secondly, to ensure that the gadolinium thickness and required uniformity (better than 5 %) could be accurately and repeatedly attained. The first depositions of gadolinium on silicon appeared successful, but spontaneous delamination of the films occurred over a period of weeks to several months. It was not possible to correlate the delamination with sample conditions or growth parameters. Delamination is typically an artifact of residual stress in the film and can be overcome by either reducing this stress or by increasing the adhesion of the film to the substrate. Heat treatment and aggressive surface cleaning processes were not considered for fear of damaging the PImMS sensor architecture. Instead, film adhesion was increased via transition-metal pre-sputter preparation. Fig 3 below shows a typical depth profile measurement and Fig 4 is a SEM image showing that a smooth homogenous thin-film has been obtained.

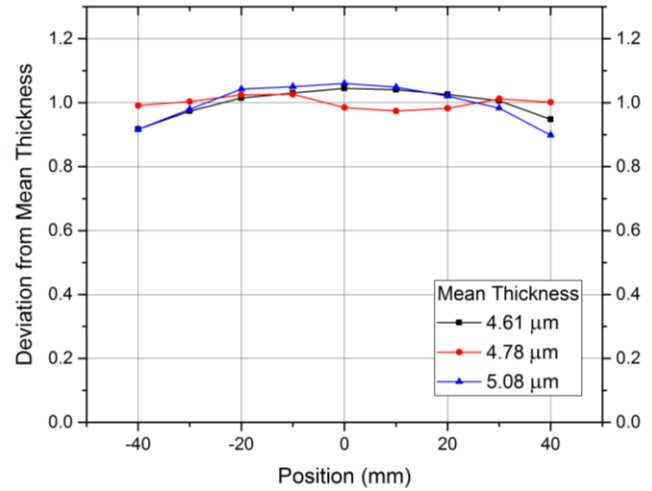


Fig 3. Typical depth profile for thin-film Gd, sputtered on Ø50 mm test wafer. Data is normalized to emphasize relative changes in thickness. Note the PImMS-2 sensor would cover the central portion of this scan as it is approximately 22 mm x 22 mm in size.

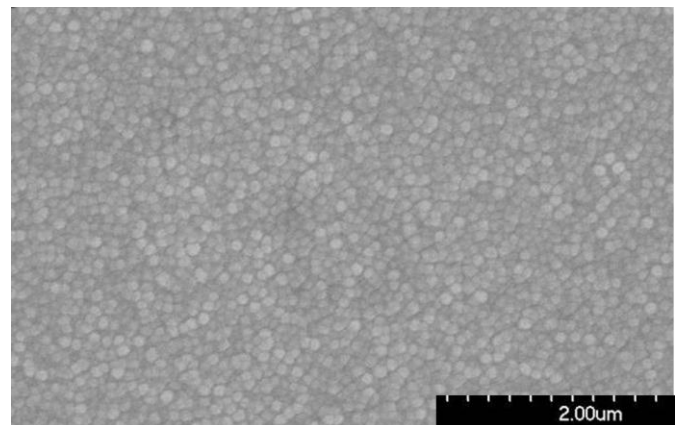


Fig 4. SEM image of sputtered Gd thin-film. High aspect ratio structures were not observed and the surface is highly homogenous. The full-scale of the black bar is 2 μm.

#### D. Camera Hardware

The PImMS sensor is housed in a bespoke camera designed by Aspect Systems GmbH. The camera consists of a mechanical enclosure containing a system of modular electronics. For neutron detection, no optical components are used.

The functions of the electronics are to (a) mount and power the sensor, (b) provide control, configuration and timing input signals to the sensor, (c) read the sensor's data outputs and (d) communicate over a USB-2 interface to a control PC. Communications between the PC and camera are further described in §V.

The control, readout and USB functions are implemented in programmable electronics (FPGAs). This has allowed tailoring of the sensor's operation to the requirements of ERNR operation, such as reading out a variable number of pixel registers (§V.A.) and implementing a variable time structure of measurements (§V.B)

#### E. Software and Data Reduction

The camera is controlled using bespoke software written in LabVIEW 2013, with a graphical user interface (GUI) that allows the user to change the operational parameters. Examples of user-adjustable settings include altering the time bin width, the frame length and parameters controlling the pixel sensitivity to achieve the best signal/noise ratio for the experiment and beam line conditions. The GUI also allows online analysis, including visualization of the neutron time-of-flight spectrum and visualization of the image being acquired. Images can be viewed on a frame-by-frame basis or cumulatively. Data can be saved in either ASCII text format for convenience or as binary data. ASCII writes an  $(x, y, t, f, r)$  data point for each detected neutron, with  $x$  and  $y$  specifying the pixel,  $t$  the integer time-code value,  $f$  the frame, and  $r$  identifying which of the four registers is being read. Within a given experiment the data points are appended to the accumulating data file on each acquisition cycle. When employing binary data format, the software similarly records rows of unsigned 16-bit integers for  $(x, y, t)$  data points, appending the data set after each frame. For the binary file, the data array is prepended with two 32-bit integers describing the dimensions of the array, allowing the data corresponding to different frames to be separated. Data recorded in binary provides a significant improvement in read/write speed as well as a footprint typically 20 % of the data file size recorded in ASCII.

Offline analysis of the data is performed using a suite of bespoke software also written in LabVIEW 2013. Common post-processing steps include: noise filtration, image compilation over particular time-of-flight ranges, time-of-flight extraction for individual regions-of-interest and open-beam correction. The analysis software operates by reading data from each neutron pulse, analyzing it, discarding it from memory, then reading in the next data stream meaning that the computational memory requirements are independent of the size of the data set. Consequently, data sets with sizes in

excess of 50GB (binary format) have been recorded and analyzed without difficulty, with no limitations on the maximum data set size anticipated up to the 64-bit limit.

During the development phase these programs were developed as required. However, the data reduction and initial analysis process are currently being implemented within the Mantid [32] software suite.

### V. DETECTOR OPERATION AND FUNCTIONALITY

#### A. Sensor and Camera Readout

Each of the four memory registers in each pixel can be read out independently of the others. For example, it is possible to read out memory register  $x$  of every  $n$ th pixel. While full flexibility is useful at a commissioning and diagnostic level, it can overcomplicate the set-up process for a user. Based on our experience, a set of commonly used operational modes have been implemented to allow the user to quickly and efficiently optimize the temporal structure of their measurement. The finer details of this process are explained in §V.B. Here, the point is emphasized that the sensor can operate as a 1, 2, 3 or 4 register detector, with the complete readout time (from sensor to control PC) scaling accordingly. Table 2 gives the read-out times as measured. Read-out time is currently bottle-necked by the use of USB-2 data transfer, which will be upgraded in future improvements. Readout by USB-2 has the advantage of robust plug-and-play usability, which means the detector can be run by almost any standard PC without any bespoke hardware being required.

#### B. Measurement Structure and Sampling Scheme

The term 'time windows of interest' (TWOI) is used here to describe the temporal structure of the measurement in relation to the time-of-flight (ToF) spectrum, i.e within one pulse of neutrons. GP2 is highly flexible in this regard and can operate in several different modes. When considering the best measurement strategy, the user should balance three factors against each other.

1. Where in the neutron pulse the important data is located, and what sampling rate is required.
2. How many of the 4 registers to use. If the measurement time window is over a region of low flux, it is highly unlikely that all 4 registers will be required.
3. Where in the neutron pulse to perform read-out.

The simplest case is a uniform sampling over most of the pulse. To ascertain how many registers are usefully collecting data it is beneficial to perform a short run and analyze the data. Note that consideration should be given to the data rate attained for the open beam run, not necessarily the rate for the sample measurement, in which the beam has been attenuated.

At a pulsed spallation source, the best time to perform read-out is often at the end of each neutron pulse and over the start of the next. For example, consider a measurement performed



at the IMAT beamline at ISIS, which might require three registers to measure the thermal and cold flux. As the source frequency is 10 Hz, the 15.89 ms readout could be performed in the last 5 ms of one pulse and the first 10.89 ms of the next. This is a zero-loss setup as the detector records over the neutron energies of interest and does not miss the next pulse due to readout. In this example GP2 is operating with just one TWOI, which measures with one sampling rate over the full spectrum.

A more complex scenario may be encountered in which fine sampling is required over several Bragg edges, with coarse

TABLE II  
READ-OUT TIME FOR THE GP2 DETECTOR

Number of registers read	Read-out time
4	21.19 ms
3	15.89 ms
2	10.59 ms
1	5.298 ms

The change in read-out time, as measured.

sampling in-between. For example, the bulk of the thermal flux might be recorded to produce a ‘white beam’ image with high statistical validity, but some Bragg edges might be sampled to identify the material, phase, texture or strain. In this case the user can implement several TWOIs, with different sampling rates. This is simple to implement with the detector’s software, which allows control of the number of time windows, the sampling rate and any pauses required in between. In this case, readout commences at the end of the final TWOI and continues until completion. A start-trigger received during this time will not disrupt read out. Instead the detector accepts the trigger and pauses for the length of time pre-specified by the user.

### C. Utilization of Memory Registers

The user is free to choose how many of the four registers are to be read out; balancing the cost in time spent transferring data against measurement. In some situations, the TWOI structure might remain unchanged and the registers utilized to handle an increase in flux during an experiment. For example, a standard sample-in/sample-out normalization can yield two measurements which expose the detector to significantly different fluxes, particularly if the sample is strongly absorbing. In this case, and generally speaking, the user can immediately gauge the severity of any distortion in the neutron pulse due to missed counts by observing the individual ToF spectra recorded in each register. Multiple neutrons per pixel per frame are recorded sequentially i.e. the first neutron by register one, the second by register two etc. Consequentially, the probability of a neutron being recorded in the second, third or fourth register is intrinsically weighted toward later times due to the nature of counting up from a time-zero. Or, alternatively phrased: the ToF spectra from a pixel’s four registers will not have the same shape. Their sum can be considered minimally distorted provided that the last register included is minimally occupied.

## VI. DETECTOR CHARACTERIZATION AND MEASUREMENT

### A. Neutron Efficiency

The neutron detection efficiency is dependent on the thickness of the gadolinium coating and on the neutron wavelength. Neutrons with shorter wavelength (higher energy) penetrate more deeply into the gadolinium than those with long wavelength. Consequently, as wavelength increases, so does the conversion electron (CE) emission from the back surface. This is the consequence of the mean free path of thermal neutrons in gadolinium being comparable to the mean free path of the CE spectrum, which is isotopically emitted. CE emission from the back surface will continue to increase until the point at which the majority of CEs with a backwards trajectory (with respect to the neutron velocity) are able to escape the gadolinium. Any further increase in neutron wavelength will not significantly enhance the registered counts as the neutron is absorbed very close to the gadolinium surface. Measurement of this plateau is indicative of the maximum possible efficiency for the detector in reverse geometry. The converse argument is also true; shorter wavelength neutrons will be absorbed deeper under the gadolinium surface giving a greater chance of the CEs escaping from the front surface. If the gadolinium is too thick, no CEs will escape from the front. This results in a peak in the forward CE electron emission and therefore detector efficiency as a function of wavelength, rather than a plateau.

From these geometric arguments, measuring in ‘reverse’ geometry will provide a top-limit for the efficiency curve, provided the gadolinium is thick enough to be opaque and the measurement extends to sufficiently long wavelengths. In reality the detector will have some minimum energy threshold, beneath which electrons will either fail to be recorded, or fail to make it to the detector.

When measuring in ‘reverse’ the neutron beam travels through the detector assembly before interacting with the gadolinium. This is unavoidable and must be measured and corrected for. This wavelength-dependent attenuation correction was measured using a pair of especially designed beam monitors on the ROTAX beamline at ISIS. The corrected efficiency data for a 500  $\mu\text{m}$  thick foil is shown below in Fig 5. As expected, the neutron efficiency rapidly increases with increasing wavelength due to the gadolinium absorption cross section. Above 2  $\text{\AA}$  the efficiency increases minimally, almost flattening out. Here the gadolinium cross section is following a ‘ $1/v$ ’ law, but the reducing penetration depth of the neutrons means does not result in an increase in efficiency. Measurement beyond 4  $\text{\AA}$  was not possible on the ROTAX beamline at this time with adequate statistics.

To understand this result, comparison is made with the theoretical modelling carried out by Abdushukurov *et al.* [26]. Interestingly the experimental and model data are in closest agreement at shorter wavelengths, but disagree in shape and magnitude with increasing wavelength. This is understood to be a result of the complex CE emission spectrum from

gadolinium being dominated by K and L shell emission. The reduced neutron detection efficiency, when compared to the model, indicated that the K shell CEs do not deposit enough energy into the sensor to be registered. These CEs are counted in the model data, explaining why the data is in good agreement at 1 Å.

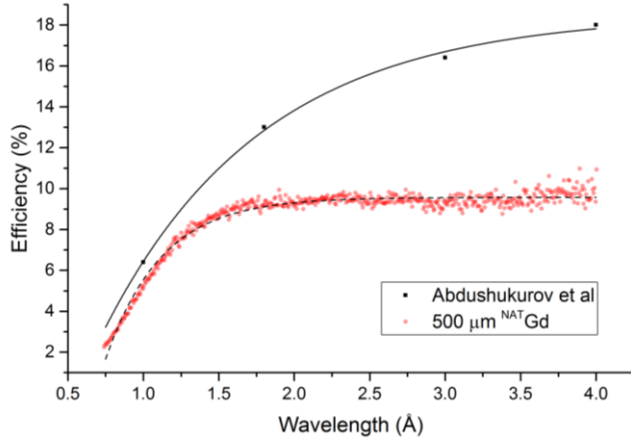


Fig 5. The neutron detection efficiency for the PImMS sensor used with a 500 μm gadolinium foil in back geometry.

Fig 5 indicates that the highest possible neutron efficiency for the GP2 sensor, using non-isotope-enriched gadolinium, is ~9.5 %. Continuing to operate in reverse geometry is not a feasible option for neutron radiography, due to the activation of the detector, the large sample-to-sensor distance and critically the structure and scattering added to the beam. To operate in forward geometry (the 'normal' geometry for a detector), 4 μm of gadolinium was deposited onto the sensor surface. Our investigations found this to be an optimum thickness for thermal wavelengths, but improvement can be expected when the detector is used on a cold-source beamline.

When quoting the neutron efficiency, it is important to report the operational conditions and the dependent parameters. Accordingly, the neutron efficiency for a 4 μm thin film is reported with the gamma sensitivity as a function of global threshold in Fig 6, which can be seen to approach 8.5 %.

### B. Gamma Sensitivity

The gamma sensitivity of the GP2 detector was measured using the Cobham RAD Solutions [33] 12TBq  $^{60}\text{Co}$  source at a source-detector distance of 3 m, ensuring a highly homogenous gamma field. The gamma flux was measured using a calibrated ion chamber. Comparison with the gamma flux recorded by the GP2 sensor yielded the gamma sensitivity. Fig 6 shows the relationship between gamma sensitivity and neutron detection efficiency, as a function of discriminator threshold. Typically the detector is run with a discriminator threshold in the region of -40 mV, which corresponds to a neutron detection efficiency of ~7.5 % and a gamma sensitivity of  $1.5 \times 10^{-3}$ .

The relative contributions of the PImMS sensor chip and the gadolinium coating to the gamma sensitivity were investigated using a partially coated sensor. For a 4 μm thin film, it was determined that the gamma sensitivity of the GP2 detector comes primarily from the PImMS sensor, with approximately a 30 % enhancement from the gadolinium coating.

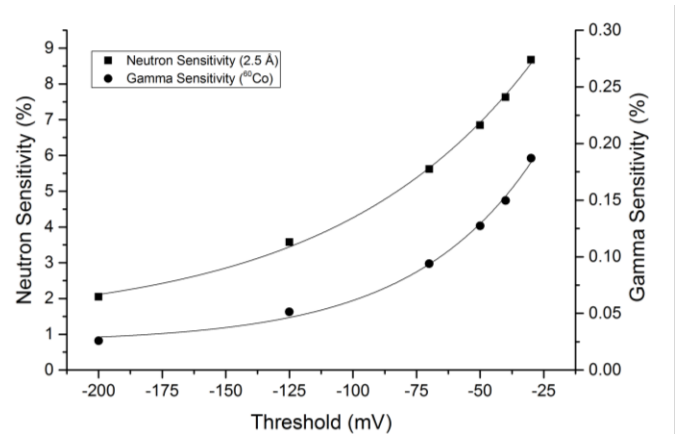


Fig 6. LEFT-Axis: the neutron detection efficiency at 2.5 Å for a 4 μm  $^{157}\text{Gd}$  thin-film. RIGHT-Axis: the gamma sensitivity for the same detector measured using  $^{60}\text{Co}$ . Both measurements are presented as a function of discriminator threshold.

### C. Spatial Resolution

The spatial resolution was determined using a quarter-Siemens star pattern, designed in-house. The star is laser ablated from a 7  $\mu\text{m}$  thick gadolinium deposition on a silicon substrate. The stenciled pattern provides an immediate estimate for the smallest distinguishable features, as well as a knife-edge to calculate the modulation transfer function in both  $x$  and  $y$  directions. Fig 7 shows the white-beam neutron radiograph for the quarter-star. The rounded edge, which fades out, is due to a thinning of the gadolinium thickness on the star itself. The modulation transfer function (MTF) at 10 % contrast was determined using the ImageJ plug-in developed at Helmholtz-Zentrum Berlin [34]. In both  $x$  and  $y$  directions, the MTF@10 % contrast was determined to be 6.4 lp/mm. Inverting and dividing by two gives 71  $\mu\text{m}$ , effectively the single pixel size. This confirms that the application of gadolinium to the PImMS CMOS has not significantly reduced the intrinsic detector resolution, a milestone result.

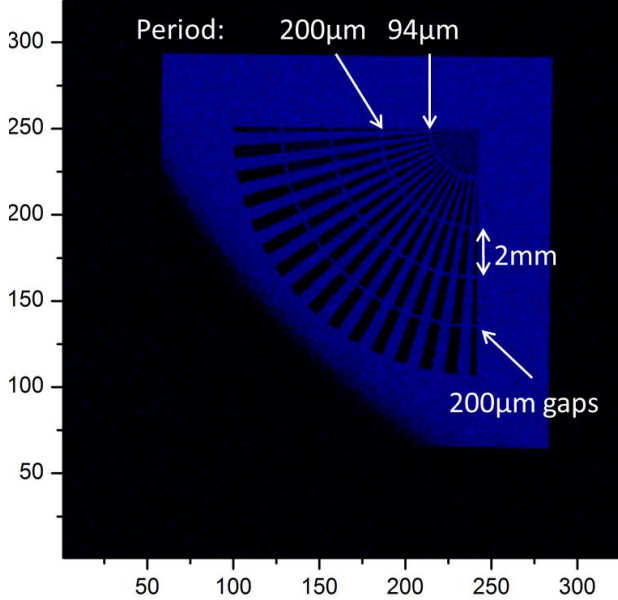


Fig 7. The ISIS quarter-Siemens star. The spoke period is shown for the two innermost segments. The axis units are pixel number, where one pixel is 70  $\mu\text{m}$ .

### D. Radiation Hardness and Induced Effects

Neutron radiation hardness has been tested throughout the development of the detector. While CMOS sensors are typically described as being ‘radiation hard’, it is hard to define a metric that allows them to be compared directly with other technologies. This is clear when one considers the different effects that high energy neutrons, thermal neutrons and gamma radiation can have on a detector. For example, CCD cameras are sensitive to gamma-induced damage, which manifests as dead pixels. To test for such effects the GP2 camera was exposed to  $>1$  kRad of  $^{60}\text{Co}$  gamma, during which no dead pixels were created and no observable performance changes were observed from the noise/thresholds scans.

ERNR is typically performed using neutrons in the wavelength range from 1  $\text{\AA}$  to 8  $\text{\AA}$ . In this energy range, neutron-induced radiation damage is not expected. Preliminary testing generally supports this. For example, over the measurement period for the dataset used to produce the tomography shown in Fig 9, the sensor was exposed to a fluence of  $>4 \times 10^{11}$  thermal neutrons. During this time no radiation induced damage was observed, nor was there any change in the measured neutron sensitivity. This is demonstrated by the tomographic dataset, which requires uniform, equivalent projections to produce a reconstruction. It should also be noted that no burn-in or memory effects have been observed; these were investigated using the LARMOR instrument at ISIS, using silver as a high contrast absorber.

The GP2 detector is not designed for neutron experiments at energies greater than 100 meV, above which the gadolinium neutron cross section reduces dramatically. Accordingly, the fast neutron radiation tolerance of the detector has not been investigated. However, the GP2 detector does have some sensitivity in this range due to the high number of nuclear resonances above  $\sim 2$  eV.

## VII. MEASUREMENT OF CALIBRATION SAMPLES

### A. Bragg Edges from $\alpha$ -Fe Powder

To demonstrate the temporal resolution of the GP2 detector, transmission through a powder sample of  $\alpha$ -Fe was measured on the IMAT beamline at ISIS [35], as part of the detector commissioning programme. The sample was chosen due to the sharp, strong Bragg edge features in the ToF spectrum. Fig 8 shows the microscopic cross section,  $\sigma$ , as defined in (1) below.  $N$  is the nuclear density,  $d$  the sample thickness,  $I_0$  the open-beam spectrum and  $I_{Fe}$  the sample data, the latter two being a function of ToF. The scaling constant,  $C$ , has been introduced to facilitate comparison of the data with that calculated by nxsPlotter [36]. Absolute measurement of the microscopic cross section required additional experiment optimization beyond the scope of this measurement.

$$\sigma(\lambda) = \frac{C}{N d} \ln \left( \frac{I_0(\lambda)}{I_{Fe}(\lambda)} \right) \quad (1)$$

The good match between experiment and theory, and the sharp nature of the Bragg edges, demonstrate that the GP2 detector can sample these features accurately. To avoid



ambiguity, the data are presented without deconvolving the instrument resolution function, to which the rounded nature of the Bragg edges are attributable. For this experiment the time-bin width was set to  $\sim 10 \mu\text{s}$ , meaning a total of  $\sim 31$  ms of each neutron pulse was measured. If a higher sampling rate were required, the user could either decrease the measurement length proportionally or adopt a time-window (TWOI) structure, as discussed in §V.B. The GP2 detector can sample up to 80 MS/s (12.5 ns per sample), which is likely to be 3 orders of magnitude faster than required for Bragg edge studies.

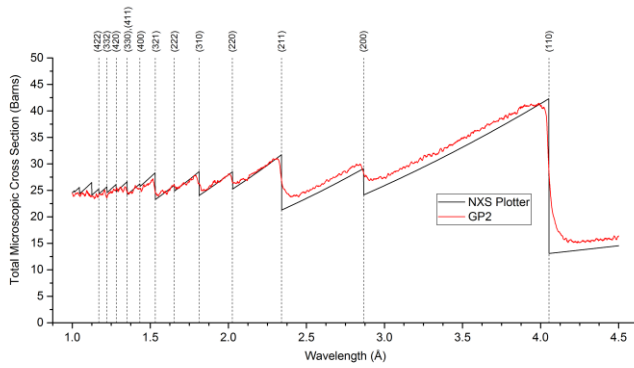


Fig 8.  $\alpha$ -Fe powder ToF spectrum measured with the GP2 detector. The positions of the indexed peaks are in good agreement with those predicted by nxsPlotter. To facilitate comparison, the GP2 data has been scaled on the y-axis, as described in the main text.

## B. Tomography

To demonstrate that the detector meets the demands for tomographic reconstruction, a sample containing a set of engineering materials, namely steel, copper and brass was measured. The sample included a mix of highly symmetric objects, such as steel ball bearings, and high aspect ratio shapes such as a copper nail. Many of these shapes are considered ‘standards’ by the neutron imaging community, as they provide quantification of the capabilities of the detector and the measurement process. The copper and steel objects were completely embedded in an aluminum matrix. As this experiment was designed to characterize the ability of the GP2 detector to acquire data of high enough quality for 3D reconstruction to be performed, rather than to perform material identification via energy-resolved methods, the data has been integrated over the full time-of-flight spectrum.

A total of 143 projections were measured, each for 30000 ISIS target station-1 frames delivered at 40 Hz. The scan angles followed the ‘golden ratio’ scan procedure, as described in [37], and covered a  $360^\circ$  scan range.

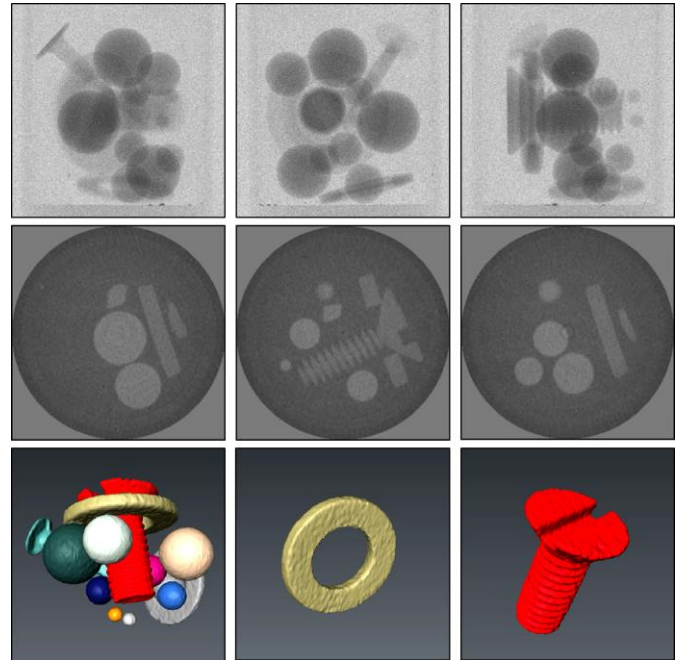


Fig 9. TOP row: Three selected projections. MIDDLE row: Three reconstruction slices. BOTTOM row: the completed tomographic reconstruction with material and shape separation, achieved via white-beam contrast segmentation.

Fig 9 shows data for each stage of the tomography measurement: radiographies, reconstructed slices and different views of the 3D rendered model. The data was of such quality that minimal ring artifacts appeared in the reconstruction and the 3D visual processing was able to complete a segmentation and surface render of all the shapes. Not only does this indicate good sample-detector alignment, it also demonstrates that the detector was stable over the measurement time and that all 143 recorded radiographies are equivalent. The measurement of the average sphere diameter in software (AVIZO Fire™) agreed with the values obtained via lab

metrology to within 2 %. The rationale for the testing of spheres, particularly touching spheres, is to validate that distortions such as stretch or skew do not feature in the final 3D render. Contrast enhancement of the image via weighted selection of time-of-flight is not presented here, as it is considered outside the scope of this instrumentation paper.

## VIII. FUTURE WORK

### A. Neutron Detection Efficiency Improvements

By imposing the condition that the GP2 detector uses thin-film  $^{157}\text{Gd}$  in forward geometry, the efficiency of the detector is limited. Further optimization of the gadolinium thickness is not expected to increase the efficiency significantly, meaning that a technology change is required in order to yield further improvement. Utilizing isotope enriched gadolinium will in theory double the detector efficiency. While this remains an attractive option, the price is likely to be prohibitive. The production of a sputter-target typically requires more than 100 grams of raw material. A market survey of suppliers of  $^{157}\text{Gd}$  performed in 2014 gave prices ranging between 5 and 12 USD per mg, depending on enrichment level, minimum quantities ordered, and form, either metal or oxide powder. While it is unlikely that the price of such a resource will reduce dramatically, the potential use of enriched gadolinium is still being investigated. The total mass of gadolinium deposited on the sensor is  $\sim 15$  mg, meaning that if a low-loss deposition method can be developed then the use of enriched gadolinium would be viable.

Efficiency improvements can also be achieved via multiple neutron conversion layers. This has been developed already as a two-layer device in the form of a ‘sandwich’ structure, with the abbreviation GP2S. The GP2S detector uses a thinned PImMS sensor (achieved via back-grinding) and two layers of gadolinium. The front layer is still a thin-film, while the back layer is thick enough to absorb all remaining neutrons. The incident neutron beam is in forward geometry for the thin layer, and effectively in reverse geometry for the second, thicker layer. Provided that the PImMS sensor is less than  $\sim 30$   $\mu\text{m}$  in total thickness, the CEs will deposit approximately equivalent energy in the depletion region. While this device has been successfully manufactured, it has not yet been fully characterized. Future work on this sensor will be reported in due course. Potentially, the GP2S sensor will combine the efficiencies reported here for both forwards and reverse geometry, although this requires experimental validation.

### B. Readout-time Improvements

The current full-sensor readout time of 22 ms does not limit the detector capability at ISIS, where the two sources operate at 40 Hz and 10 Hz. The 40 Hz source neutron intensity does not challenge the 4-register capability of the GP2 detector, so it can comfortably operate as a one or two register camera, reducing read-out time and enabling 40 Hz operation. At the 10 Hz source, where the flux generated is generally an order of magnitude larger, there is ample time within the 100 ms

frame length to read out the detector. Clearly, other source structures may not fall neatly into one or other of these two categories, and in the future there may be a demand for reduced readout time. Similar challenges may arise when the proposed improvements to the neutron detection efficiency are realized. In this case there exists the option of multi-tap readout from sensor to camera, and the option of implanting either CameraLink or USB-3 data transfer to PC. Implementing this option would reduce the four-register readout time to  $\sim 2.8$  ms.

### C. Toward Large Area Coverage

The PImMS sensor contains over 600 transistors within each individual pixel, providing the required logic for it to operate as an event-mode sensor. CMOS architecture is substantially more complex than that of a CCD or silicon drift detector and as such has different limitations. The PImMS architecture can be thought of as effectively transferring a large part of the driving and control electronics to within every individual pixel. Due to the complexity of this type of sensor, scaling up in size is generally problematic, as the yield (viable devices per foundry production run) decreases with increasing area. Combining the considerations of yield, sensor layout, and production cost with the requirements of ERNR, it is proposed that the PImMS sensor should be enlarged in one direction only. The larger sensor would have an active area of approximately 22 mm x 97 mm. Making the sensors 1-side buttable would allow them to be mounted as continuous bars, measuring 22 mm x 194 mm. The sensors are then tiled in an alternating gap/bar pattern, where 50 % of the area is not sampled. To fill in the missing stripes in detector coverage, the sample or detector would have to be translated by 22 mm once. Although the measurement time is doubled, the full area would be covered and the stitched data set would be gapless.

## IX. CONCLUSION AND OVERVIEW

The thorough characterization reported here demonstrates that the GP2 detector is a suitable candidate for ERNR at a spallation source. Detector properties such as gamma sensitivity, neutron efficiency and spatial resolution have been accurately determined and are well matched to the initial specification. The novel properties of the detector, such as the ability to place the detector extremely close to the sample, continuous sensitive area, and four memory registers per pixel, place the detector in a unique category within ERNR. For this reason it is expected that the detector will facilitate the measurement of novel and demanding samples, particularly those that are weakly attenuating, resulting in a large neutron flux, or where a very small sample-detector distance is required.

Future development of the GP2 detector will focus on increasing the neutron detection efficiency and increasing the sensitive area. A multi-layered device has already been prototyped, which will increase detector efficiency, while the increase in active area will likely be achieved either via sparse-tiling of several sensors or in a new version of the

PImMS sensor.

The current version of the GP2 detector is being implemented within the IMAT detector suite at ISIS, with the aim of using the detector in the upcoming user cycles.

## X. REFERENCES

- [1] H. Kallmann, "Neutron Radiography," *Research*, vol. 1, p. 254, 1948.
- [2] J. S. Brenizer, "A review of significant advances in neutron imaging from conception to the present," *Phys Proc*, vol. 43, p. 10, 2013.
- [3] I. Manke, H. Markötter, T. Arlt, C. Tötze, M. Klages, J. Haußmann, S. Enz, F. Wieder, J. Scholta, N. Kardjilov, A. Hilger and J. Banhart, "Fuel Cell Research with Neutron Imaging at Helmholtz Centre Berlin," *Physics Procedia*, vol. 69, p. 619, 2015.
- [4] R. Satija, D. L. Jacobson, M. Arif and S. A. Werner, "In situ neutron imaging technique for evaluation of water management systems in operating PEM fuel cells," *Journal of Power Sources*, vol. 129, no. 2, p. 238, 2004.
- [5] A. E. Craft, D. M. Wachs, M. A. Okuniewski, D. L. Chichester, W. J. Williams, G. C. Papaioannou and A. T. Smolinski, "Neutron Radiography of Irradiated Nuclear Fuel at Idaho National Laboratory," *Physics Procedia*, vol. 69, p. 483, 2015.
- [6] M. Zarebanadkouki, Y. X. Kim and A. Carminati, "Where do roots take up water? Neutron radiography of waterflow into the roots of transpiring plants growing in soil," *New Phytologist*, vol. 199, p. 1034, 2013.
- [7] E. H. Lehmann, E. Deschler-Erb and A. Ford, "Neutron tomography as a valuable tool for the non-destructive analysis of historical bronze sculptures," *Archaeometry*, vol. 52, no. 2, p. 272, 2010.
- [8] F. Salvemini, F. Grazzi, I. Angelini, P. Vontobel, A. Vigoni, G. Artioli and M. Zoppi, "Morphological reconstruction of Roman arrowheads from Iulia Concordia: Italy," *Applied Physics A*, vol. 117, no. 3, p. 1227, 2014.
- [9] M. Laaß, "Bone-conduction hearing and seismic sensitivity of the late permian anodont Kawingasaurus fossilis," *Journal of Morphology*, vol. 276, no. 2, p. 121, 2015.
- [10] D. Schwarz, P. Vontobel, E. H. Lehmann, C. A. Meyer and G. Bongartz, "Neutron Tomography of Internal Structures of Vertebrate Remains," *Palaeontologia Electronica*, vol. 8, no. 2, p. 30A, 2005.
- [11] W. Kockelmann, G. Frei, E. H. Lehmann, P. Vontobel and J. R. Santisteban, "Energy-selective neutron transmission imaging at a pulsed source," *NIM A*, vol. 578, p. 421–434, 2007.
- [12] B. Abbey, S. Y. Zhang, W. J. J. Vorster and A. M. Korsunsky, "Feasibility study of neutron strain tomography," *Procedia Engineering*, vol. 1, p. 185, 2009.
- [13] J. R. Santisteban, L. Edwards, H. G. Priesmeyer and S. Vogel, "Comparison of Bragg-Edge neutron-transmission spectroscopy at ISIS and LANSCE," *Appl. Phys. A*, vol. 74, p. s1616, 2002.
- [14] J. R. Santisteban, L. Edwards, M. E. Fitzpatrick, A. Steuwer, P. J. Withers, M. R. Daymond, M. W. Johnson, N. Rhodes and E. M. Schooneveld, "Strain imaging by Bragg edge neutron transmission," *Nuclear Instruments and Methods A*, vol. 481, no. 1, p. 765, 2002.
- [15] Y. Le Godec, M. T. Dove, D. J. Francis, S. C. Kohn, W. G. Marshall, A. R. Pawley, G. D. Price, S. A. T. Redfern, N. Rhodes, N. L. Ross, P. F. Schofield, E. M. Schooneveld, G. Syfosse, M. G. Tucker and M. D. Welch, "Neutron diffraction at simultaneous high pressures and temperatures, with measurement of temperature by neutron radiography," *Min. Mag.*, vol. 65, p. 737, 2001.
- [16] M. Strobl, "Future prospects of imaging at spallation neutron sources," *NIM A*, vol. 604, p. 646–652, 2009.
- [17] A. S. Tremsin, J. V. Vallerger, J. B. McPhate, O. H. Siegmund, W. B. Feller, L. Crow and R. G. Cooper, "On the possibility to image thermal and cold neutron with sub-15  $\mu\text{m}$  spatial resolution," *NIM A*, vol. 592, pp. 374–384, 2008.
- [18] J. Vallerger, R. Raffanti, A. Tremsin, J. McPhate and O. Siegmund, "MCP detector read out with a bare quad Timepix at kilohertz frame rates," *Journal of Instrumentation*, vol. 6, no. 1, p. C01049, 2011.
- [19] W. Kockelman, S. Y. Zhang, J. F. Kelleher, J. B. Nightingale, G. Burca and J. A. James, "IMAT a new imaging and diffraction instrument at ISIS," *Physics Procedia*, vol. 43, p. 100, 2013.
- [20] M. Morgano, E. Lehmann and M. Strobl, "Detectors Requirements for the ODIN Beamline at ESS," *Physics Procedia*, vol. 69, p. 152, 2015.
- [21] J. D. Parker, M. Harada, H. Hayashida, K. Hiroi, K. Kai, Y. Matsumoto, T. Nakatani, K. Oikawa, M. Segawa, T. Shinohara, Y. Su, S. Zhang, S. Satoh and Y. Kiyonagi, "Counting-Type Neutron Imaging Detectors of the Energy-Resolved Neutron Imaging System RADEN at the J-PARC/MLF," *IEEE NSS MIC Conference Record*, vol. 86, p. N3AP, 2016.
- [22] J. D. Parker, M. Harada, H. Hayashida, K. Hiroi, T. Kai, Y. Matsumoto, K. Oikawa, M. Segawa, T. Shinohara, Y. Su, A. Takada, S. Zhang, T. Tanimori and Y. Kiyonagi, "Development of the Next-Generation Micro Pixel Chamber-Based Neutron Imaging Detector ( $\mu\text{NID}$ ) for Energy-Resolved Neutron Imaging with High Rate and High Spatial Resolution at the J-PARC/MLF," *IEEE NSS Conference Record*, vol. N22, p. 4, 2016.
- [23] V. F. Sears, "Neutron scattering lengths and cross sections," *Neutron News*, vol. 3, no. 3, p. 29, 1992.
- [24] A. A. Harms, T. G. Blake and J. P. Marton, "Neutron imaging with thin gadolinium converters," *Nuclear Instruments and Methods*, vol. 109, no. 2, p. 253, 1973.
- [25] A. A. Harms and G. McCormack, "Isotopic conversion in

- Gadolinium-exposure neutron imaging," *Nuclear Instruments and Methods in Physics Research*, vol. 118, p. 583, 1974.
- [26] D. A. Abdushukurov, Gadolinium Foils as Converters of Thermal Neutrons in Detectors of Nuclear Radiation, Nova Science Publishers, 2010.
- [27] R. L. Varner, J. R. Beene and P. S. Friedman, "Gadolinium thin foils in a plasma panel sensor as an alternative to  $^3\text{He}$ ," *IEEE NSS Conference Record*, Vols. N41-174, p. 1130, 2010.
- [28] D. Pfeiffer, F. Resnati, J. Birch, M. Etxegarai, R. Hall-Wilton, C. Höglund, L. Hultman, I. Llamas-Jansa, E. Oliveri, E. Oksanen, L. Robinson, L. Ropelewski, S. Schmidt, C. Streltsov and P. Thuiner, "First measurements with new high-resolution gadolinium-GEM neutron detectors," *Journal of Instrumentation*, vol. 11, no. 5, p. 05011, 2016.
- [29] D. A. Abdushukurov, "Mathematical modeling of the efficiency gadolinium based neutron converters," *Applied Mathematics*, vol. 4, p. 27, 2013.
- [30] J. J. John, M. Brouard, A. Clark, J. Crooks, E. Halford, L. Hill, J. J. W. Lee, A. Nomerotski, R. Pisarczyk, I. Sedgwick, C. S. Slater, R. Turchetta, C. Vallance, E. Wilman, B. Winter and W. H. Yuen, "PImMS, a fast event-triggered monolithic pixel detector with storage of multiple timestamps," *JINST*, vol. 7, p. C08001, 2012.
- [31] I. Sedgwick, A. Clark, J. Crooks, R. Turchetta, L. Hill, J. J. John, A. Nomerotski, R. Pisarczyk, M. Brouard, S. H. Gardiner, E. Halford, J. W. Lee, M. L. Lipciuc, C. Slater, C. Vallance, E. S. Wilman, B. Winter and W. H. Yuen, "PImMS: A self-triggered, 25ns resolution monolithic CMOS sensor for Time-of-Flight and Imaging Mass Spectrometry," *IEEE NEWCAS*, 2012.
- [32] J. Taylor, O. Arnold, J. Bilheux, A. Buts, S. Campbell, M. Doucet, N. Draper, R. Fowler, M. Gigg, V. Lynch, A. Markvardsen, K. Palmen, P. Parker, P. Peterson, S. Ren, M. Reuter, A. Savici, R. Taylor, R. Tolchenov, R. Whitley, W. Zhou and J. Zikovsky, "Mantid, A high performance framework for reduction and analysis of neutron scattering data," *Bulletin of the American Physical Society*, vol. 57, 2012.
- [33] J. Hofman, A. Holmes-Siedle, R. Sharp and J. Haze, "A Method for In-Situ, Total Ionising Dose Measurement of Temperature Coefficients of Semiconductor Device Parameters," *IEEE Transactions on Nuclear Science*, vol. 62, p. 2525, 2015.
- [34] S. H. Williams, A. Hilger, N. Kardjilov, I. Manke, M. Strobl, P. A. Douissard, T. Martin, H. Riesemeier and J. Banhart, "Detection system for microimaging with neutrons," *JINST*, vol. 7, p. P02014, 2012.
- [35] W. Kockelman, G. Burca, J. F. Kelleher, S. Kabra, S.-Y. Zhang, J. Rhodes, E. M. Schooneveld, J. Sykora, D. E. Pooley, J. B. Nightingale, F. Aliotta, R. C. Ponterio, G. Salvato, D. Tresoldi, C. Vasi, J. B. McPhate and A. S. Tremsin, "Status of the Neutron Imaging and Diffraction Instrument IMAT," *Physics Procedia*, vol. 69, p. 71, 2015.
- [36] M. Boin, "nxs: a program library for neutron cross section calculations," *Journal of Applied Crystallography*, vol. 45, p. 603, 2012.
- [37] T. Kohler, "A projection access scheme for iterative reconstruction based on the golden section," *IEEE NSS Conference Record*, vol. 2004, p. 3961, 2004.
- [38] M. Strobl, C. Grünzweig, A. Hilger, I. Manke, N. Kardjilov, C. David and F. Pfeiffer, "Neutron Dark-Field Tomography," *Phys. Rev. Lett.*, vol. 101, no. 12, p. 123902, 2008.